CHAPTER IV

RESULTS AND DISCUSSION

In the following discussion each perovskite compound is indicated by the abbreviation using the initial letters of each metal in A and B sites sequentially, followed by corresponding number which refers to the proportion of each metal in the compound. For example, $La_{0.8}Sr_{0.2}Co_{0.6}Fe_{0.4}O_{3-\delta}$ and $La_{0.6}Sr_{0.4}CoO_{3-\delta}$ are abbreviated as LSCF8264 and LSC64, respectively.

4.1 Tolerance number of perovskite compounds.

The tolerance numbers of all perovskite compounds prepared are shown in Table 4.1.

Table 4.1 Tolerance number of prepared perovskites

Compounds	Tolerance No.	Compounds	Tolerance No.
LSCF8264	1.39	BSC82	1.47
LSGF6437	1.41	BSC73	1.46
BSCF5582	1.45	BSC64	1.45
LSC82	1.37	BSC55	1.44
LSC73	1.38	BSC46	1.43
LSC64	1.38	BSF82	1.51
LSC55	1.38	BSF73	1.50
LSC46	1.39	BSF64	1.49
LSF82	1.40	BSF55	1.48
LSF73	1.41	BSF46	1.47
LSF64	1.41		
LSF55	1.42		
LSF46	1.42		

These perovskite had tolerance number more than 1.00, which meant that they all should have a pseudo-cubic structure. This might be due to the substitution of the A-site cation generally distorts the BO_3 skeletal sublattice in order to attain optimal A-O bond lengths where the lower limits for cationic radii are $r_A > 0.09$ nm. When this distortion is too large, order crystrall geometries such as orthorhombic or rhombohedral become favorable.

4.2 Characterization of the perovskite compounds

For the synthesis study, the calcinations and sintering process are concerned. The effect of calcination process is in general favorable, predictable and related to the improvement of crystalline structure of as-synthesized powders. This process also removed residual water and other impurities. In case of sintering process, the effect of heat treatment is related to the substantial changes in all powder microstructures.

The synthesized perovskite compounds, substrate and catalytic perovskites, were characterized the structure by XRD and the surface morphology by SEM.

4.2.1 X-ray diffraction (XRD)

XRD was used to indicate the formation of the perovskite-type phase with either a cubic or distorted cubic structure. The lattice parameter of synthesized perovskites based on their structure was calculated by XRD software.

#### 4.2.1.1 The substrate perovskite compounds

The substrate perovskite compounds were prepared by modified citrate method. The conditions which were used to prepare the powders and membranes were shown in Table 4.2.

**Table 4.2** Physical property of the substrate perovskite compounds

Compounds	Calcination temperature, Time	Sintering temperature, Time	Observed phase after sintering	Bulk density (g/cm^3)
LSCF8264	800 ^{o}C, 4hr.	1,300 ^{o}C, 10hr.	Single phase	4.980
LSGF6437	1,000 ^{o}C, 5 hr.	1,300 ^{o}C, 10hr.	Single phase	5.052
BSCF5582	1,000 ^{o}C, 5hr.	1,100 ^{o}C, 10hr.	Single phase	6.130

Tanyong et. Al. [55] was the research group to report that the single phase of LSGF6437 powder was obtained by modified citrate method. They were also found that the prepared membranes had the high density. From the table 4.2, it is clearly shown that the single phase of LSGF powder and the dense membrane were obtained as Tanyong's report. The LSCF8264 and BSCF5582 membranes also had the single phase structures after sintered at 1,300 ^{o}C and 1,100 ^{o}C, respectively. Comparing with the solid state synthesis method done by Shoa [56] and Xu [57] who synthesized the single phase LSCF8264 and BSCF5582 after sintered at 1,500 ^{o}C and 1,150 ^{o}C respectively, the modified citrate method seems to be suitable for synthesizing the single phase of these powders under milder condition.

The XRD patterns of the LSCF8264, LSGF6437, and BSCF5582 substrate powders after calcinations were illustrated in Figures 4.1-4.3.
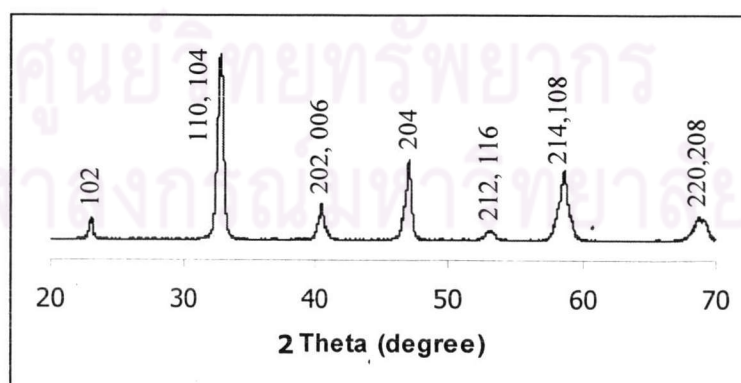

Figure 4.1 XRD pattern of LSCF8264 perovskite compound.

For LSCF8264, the XRD pattern shows a rhombohedral structure which is exhibited the diffraction lines at the reflective planes 012, 110, 104, 202, 006, 204, 212, 116, 214, 108, 220, and 208.
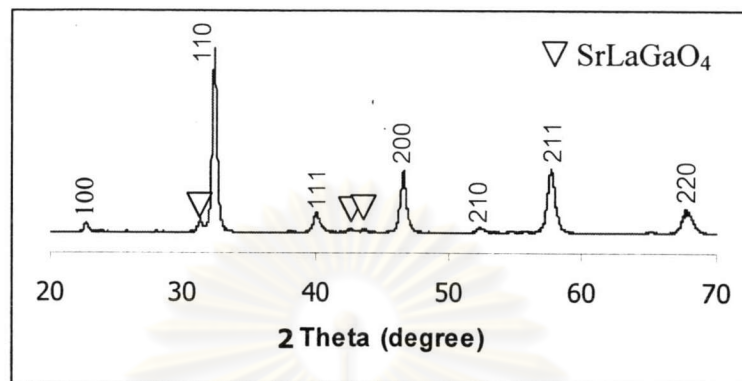
Figure 4.2 XRD pattern of LSGF6437 perovskite compound.

In this case of LSGF6437, (Figure 4.2), the powder with a cubic structure exhibited the diffraction lines at the reflective planes 100, 110, 111, 200, 210, 211, and 220. The appearance of the small peaks at $2\theta = 31$, 42, and 43 indicated the existence of trace of secondary phase ($SrLaGaO_4$). However, the trace of secondary phase disappeared after LSGF6437 membrane was sintered at 1,300 ^oC [55].
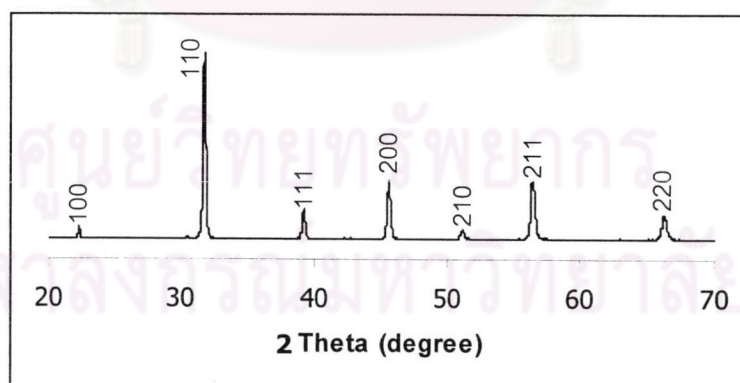
Figure 4.3 XRD pattern of BSCF5582 perovskite compound.

XRD pattern of BSCF powder after calcination at 1,000 ^oC for 5 hours was shown in Figure 4.3. This Figure was clearly shown the diffraction lines at reflective planes 100, 110, 111, 200, 210, 211, and 200. There diffraction peaks were indexed

on the basis of a cubic structure therefore the single phase perovskite with a cubic structure of BSCF5582 powder was obtained. By XRD calculation, the crystal parameter of BSCF powder is a = 3.9795 Å [58].

4.2.1.2 Catalytic perovskite compounds

The catalytic perovskite compounds were prepared by using the same method as the substrate compounds. All compounds, $La_{1-x}Sr_xCoO_{3-\delta}$, $La_{1-x}Sr_xFeO_{3-\delta}$, $Ba_{1-x}Sr_xCoO_{3-\delta}$, and $Ba_{1-x}Sr_xFeO_{3-\delta}$ (x = 0.2 - 0.6) were prepared to acquire single phase by varying calcination temperatures at 800 - 1,100 °C.

A. $La_{1-x}Sr_xCoO_{3-\delta}$ (x = 0.2 - 0.6) catalytic perovskite compounds

From XRD analysis, the effect of calcinations temperature on the phase transformation of $La_{1-x}Sr_xCoO_{3-\delta}$ (X = 0.2 - 0.6) was shown in Table 4.3. After calcinations, all characteristic peaks of all compounds became more intense and sharp. This indicated that all calcined compounds had more crystalline structure than the uncalcined compounds as mentioned above. The LSC82 and LSC73 powders calcined at the temperature in the range of 800 – 1,000 °C had the mixed phases of the secondary phase, which was due to $SrCO_3$ and perovskite phase. As the calcination temperature increased, $SrCO_3$, impurity decreased but it was still retained. For LSC 64, LSC55, and LSC46, the powders calcined at 800 °C also show the mixed phases while the single phase perovskite can be obtained after calcination at 900 °C for LSC55 and LSC46 and 1,000 °C for LSC64, respectively. This might be possible that the increase in Sr content causes the decrease in $SrCO_3$ impurity and the lower the calcination temperature.

Table 4.3 Existence of the observed phase of $La_{1-x}Sr_xCoO_{3-\delta}$

Compounds	Observed phase (cal. 800 ^{O}C, 4 hr.)	Observed phase (cal.900 ^{O}C, 4 hr.)	Observed phase (cal.1,000 ^{O}C, 5 hr.)
LSC82	Trace of secondary phase	Trace of secondary phase	Trace of secondary phase
LSC73	Trace of secondary phase	Trace of secondary phase	Trace of secondary phase
LSC64	Trace of secondary phase	Trace of secondary phase	Single phase
LSC55	Secondary phase	Single phase	-
LSC46	Secondary phase	Single phase	-

XRD patterns of the $La_{1-x}Sr_xCoO_{3-\delta}$ (x = 0.2 - 0.6) samples were shown in Figure 4.4.
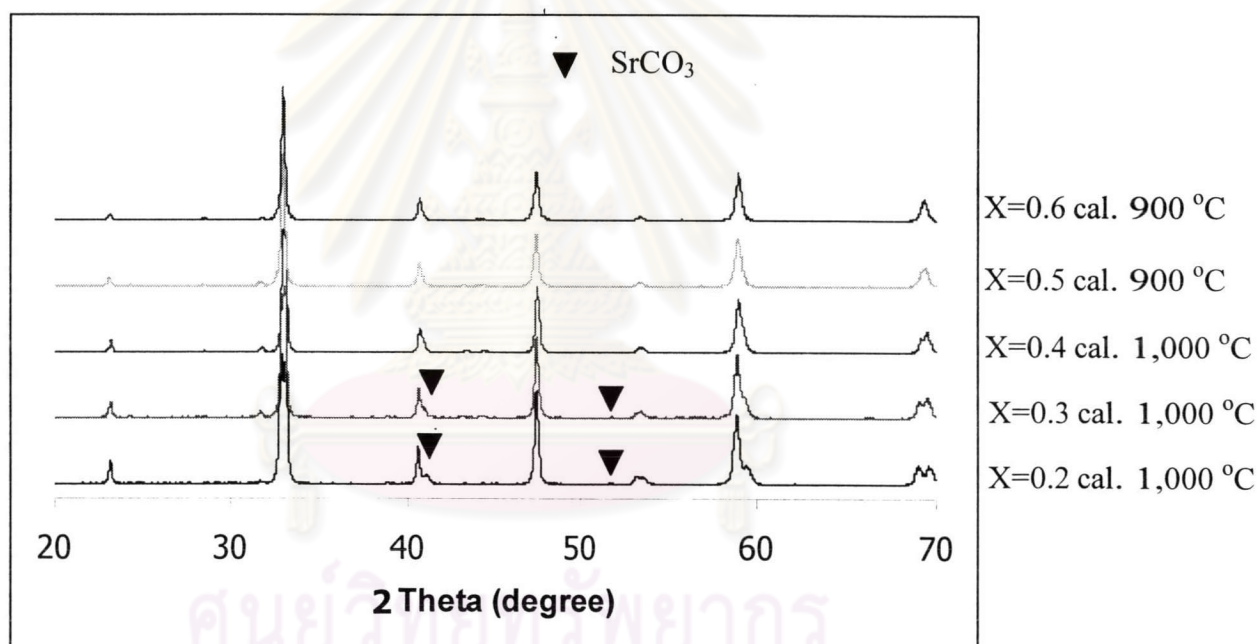
Figure 4.4 XRD patterns of $La_{1-x}Sr_xCoO_{3-\delta}$ (x = 0.2 - 0.6) catalytic perovskite compounds after calcined.

The XRD patterns of $La_{1-x}Sr_xCoO_{3-\delta}$ when the Sr content was higher than 0.4 (x ≥ 0.4) showed the single phase perovskite at 900 ^{o}C and 1,000 ^{o}C when the Sr content was less than 0.3 (x ≤ 0.3), the secondary phase appeared. For the sample, x ≤ 0.3 even though the calcination temperature was increased to 1,000 ^{o}C, the secondary

phase was formed. Therefore, LSC55, LSC64, and LSC46 were used for coating the membranes.

B. La$_{1-x}$Sr$_x$FeO$_{3-\delta}$ (x = 0.2 - 0.6) catalytic perovskite compounds

In Table 4.4, it was shown that the single phase perovskite of LSF73 and LSF82 were obtained after calcined at 800 ^{o}C and 1,000 ^{o}C, respectively.

Table 4.4 Existence of the observed phase of La$_{1-x}$Sr$_x$FeO$_{3-\delta}$

Compounds	Observed phase (cal. 800 ^{o}C, 4 hr.)	Observed phase (cal. 900 ^{o}C, 4 hr.)	Observed phase (cal. 1,000 ^{o}C, 5 hr.)
LSF82	Trace of secondary phase	Trace of secondary phase	Single phase
LSF73	Single phase	-	-
LSF64	Trace of secondary phase	Trace of secondary phase	Trace of secondary phase
LSF55	Trace of secondary phase	Trace of secondary phase	Trace of secondary phase
LSF46	Trace of secondary phase	Trace of secondary phase	Trace of secondary phase

The secondary phase of SrFeO$_3$-data base: (JCPDS 40-0905) [59], observed in XRD patterns of LSF64, LSF55, and LSF46, was decreased after calcination at 1,000 ^{o}C.

The XRD patterns of La$_{1-x}$Sr$_x$FeO$_{3-\delta}$ (x = 0.2 - 0.6) compounds after calcined at optimum temperature were shown in Figure 4.5.

ศูนย์วิทยทรัพยากร

จุฬาลงกรณ์มหาวิทยาลัย
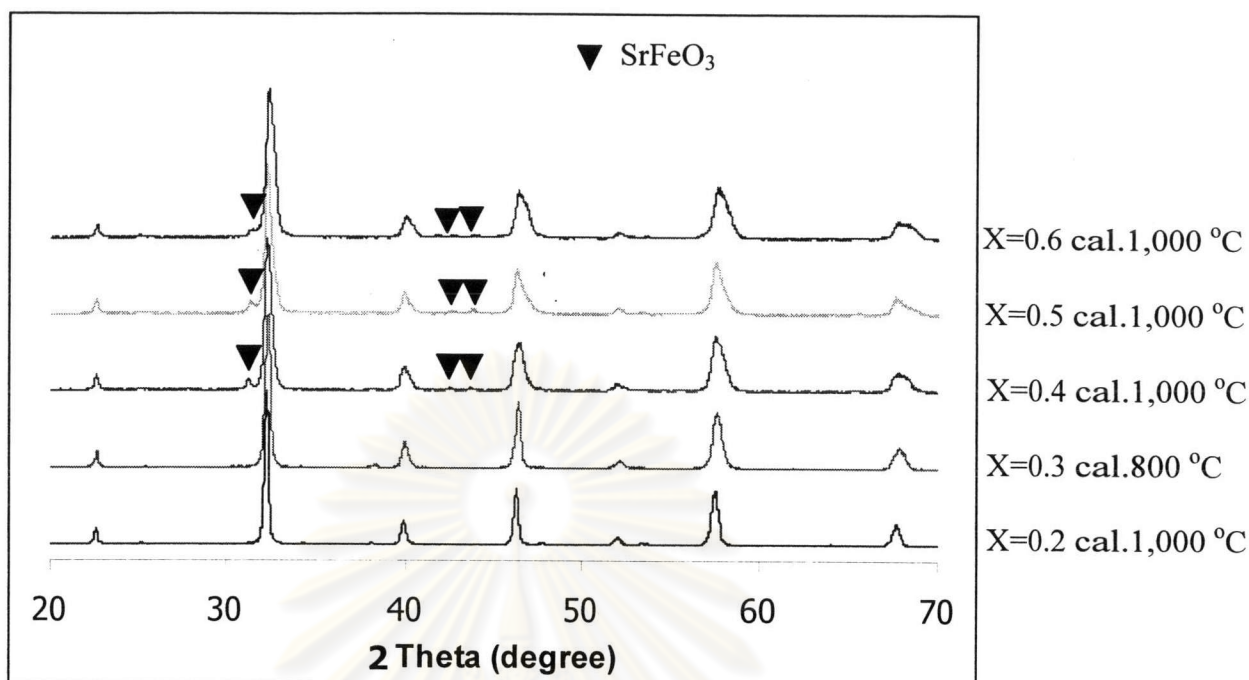
Figure 4.5 XRD patterns of $La_{1-x}Sr_xFeO_{3-\delta}$ (x = 0.2 - 0.6) catalytic
perovskite compounds after calcined.

The sharp well-defined peaks of perovskite phase of $La_{1-x}Sr_xFeO_{3-\delta}$ were
acquired when x = 0.2 and 0.3. The XRD patterns of the synthesized $La_{1-x}Sr_xFeO_{3-\delta}$
(x = 0.2 - 0.6) samples showed that the secondary phases were detected when the
amount of Sr content was higher than 0.4 (x ≥ 0.4). In the case of the relationship
between the amount of Sr content and the obtained single phase structure,
$La_{1-x}Sr_xFeO_{3-\delta}$ series exhibited the opposite phenomenon as LSC series. The single
phase structure was obtained when the high amount of Sr content was used in LSF
series and vice versa in LSC series. The reason should be further studied. Therefore,
LSF82 and LSF73 were used for coating the membranes.

C. $Ba_{1-x}Sr_xCoO_{3-\delta}$ (x = 0.2 - 0.6) catalytic perovskite compounds

In order to obtain the single phase of $Ba_{1-x}Sr_xCoO_{3-\delta}$, the powders were
calcined at different temperatures 800 °C, 1,000 °C, and 1,100 °C. The phase
formations of BSC were shown in Table 4.5. It was found that the BSC64, BSC55,

and BSC46 powders had the single phase perovskite structure after calcination at 1,000 °C.

Table 4.5 Existence of the observed phase of $Ba_{1-x}Sr_xCoO_{3-\delta}$

Compounds	Observed phase (cal. 800 °C, 4 hr.)	Observed phase (cal. 1,000 °C, 5 hr.)	Observed phase (cal.1,100 °C, 5 hr.)
BSC82	Secondary phase	Secondary phase	Secondary phase
BSC73	Secondary phase	Trace of secondary phase	Trace of secondary phase
BSC64	Secondary phase	Single phase	-
BSC55	Secondary phase	Single phase	-
BSC46	Secondary phase	Single phase	-

XRD patterns of $Ba_{1-x}Sr_xCoO_{3-\delta}$ (x = 0.2 - 0.6) compounds were shown in Figure 4.6.
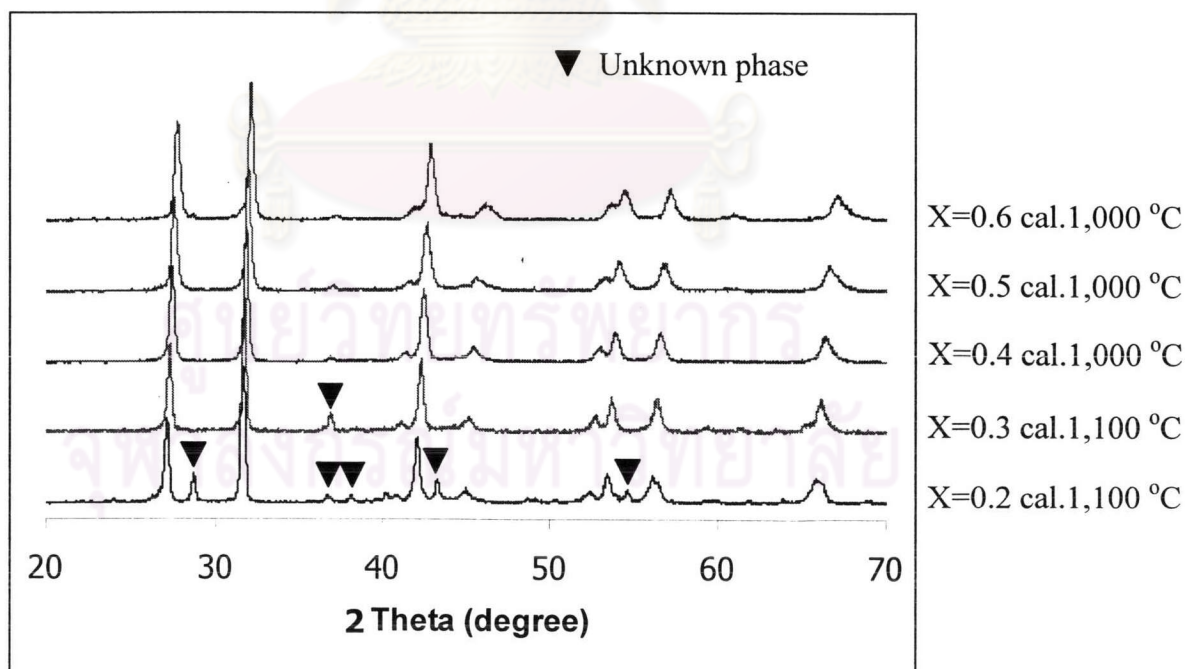
Figure 4.6 XRD patterns of $Ba_{1-x}Sr_xCoO_{3-\delta}$ (x = 0.2 - 0.6) catalytic perovskite compounds after calcinations.

It was indicated that the XRD peaks of $Ba_{1-x}Sr_xCoO_{3-\delta}$ were shifted toward higher angles with the Sr doping. The single phase of perovskite structure was found for x = 0.6, 0.5, and 0.4, while unknown phases which could not be identified, were appeared for x = 0.3 and 0.2.

Therefore, BSC64, BSC55, and BSC46 were used for coating the membranes.

D. $Ba_{1-x}Sr_xFeO_{3-\delta}$ (x = 0.2 - 0.6) catalytic perovskite compounds

The observed phase of $Ba_{1-x}Sr_xFeO_{3-\delta}$ powders calcined at various temperatures (800 °C, 1,000 °C, and 1,100 °C) were listed in Table 4.6.

Table 4.6 Existence of the observed phase of $Ba_{1-x}Sr_xFeO_{3-\delta}$

Compounds	Observed phase (cal. 800 °C, 4 hr.)	Observed phase (cal. 1,000 °C, 5 hr.)	Observed phase (cal.1,100 °C, 5 hr.)
BSF82	Secondary phase	Trace of secondary phase	Single phase
BSF73	Secondary phase	Secondary phase	Single phase
BSF64	Secondary phase	Trace of secondary phase	Single phase
BSF55	Secondary phase	Single phase	-
BSF46	Secondary phase	Trace of secondary phase	Trace of secondary phase

BSF82, BSF73, and BSF64 perovskites were obtained as single phases after calcined at 1,100 °C. XRD pattern of BSF55 showed a single phase at 1,000 °C. For BSF46, trace of secondary phase was still remained after calcined at 1,100 °C. There results show that the single phase perovskite of all powders was obtained except for x = 0.6. Figure 4.7 shows XRD patterns of $Ba_{1-x}Sr_xFeO_{3-\delta}$ (x = 0.2 - 0.6) powders.
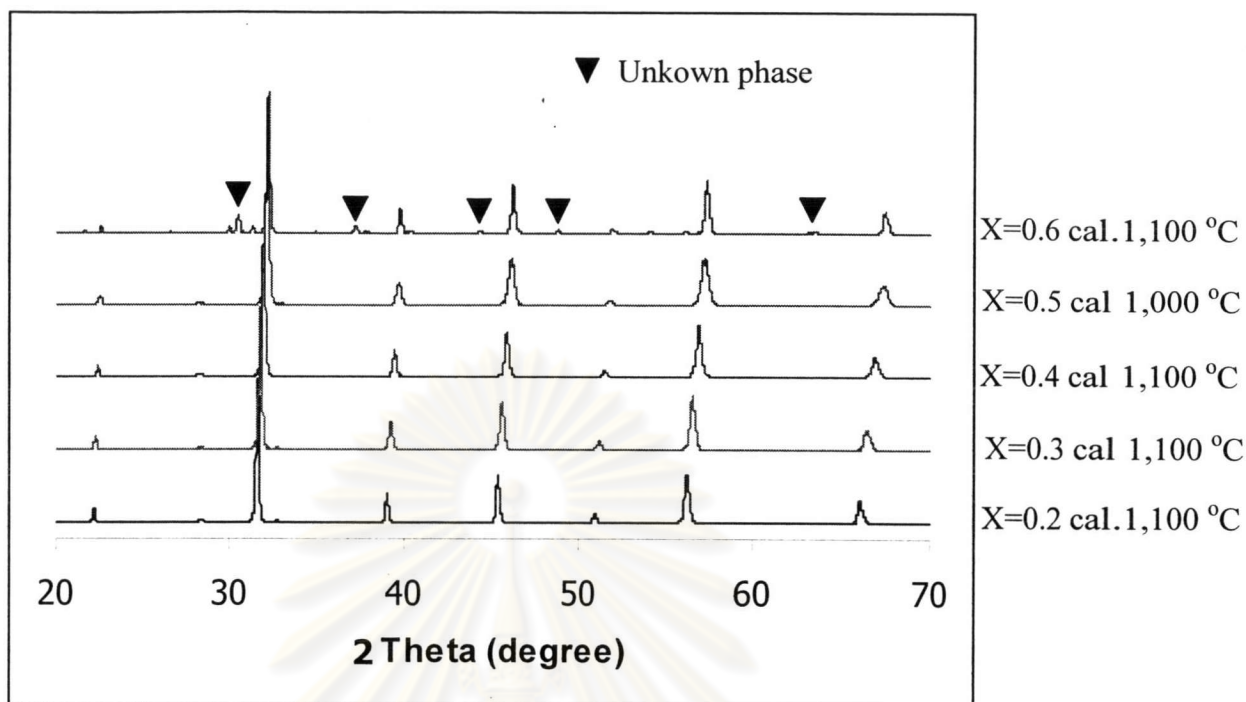
**Figure 4.7** XRD patterns of $Ba_{1-x}Sr_xFeO_{3-\delta}$ (x = 0.2 - 0.6) catalytic perovskite compounds after optimum calcined temperatures.

For $Ba_{1-x}Sr_xFeO_{3-\delta}$ with x = 0.2 - 0.6, all peaks shifted toward higher angles when the amounts of Sr content increased. The shift of XRD peak to higher angle in BSC and BSF series can be explained in term of ionic radius. Generally, the replacement of Ba^{2+} (r_{Ba2+} = 1.61Å) with the smaller cation, Sr^{3+} (r_{La3+} = 1.36Å) will lead to increase the degree of 2θ and to decrease the lattice parameter. Therefore, BSF82, BSF73, BSF64, and BSF55 were choosed for coating the membranes.

4.2.1.3 The influence of calcination temperature on phase purification

Figure 4.8 shows the effect of calcinations temperature on phase purity of LSC64.
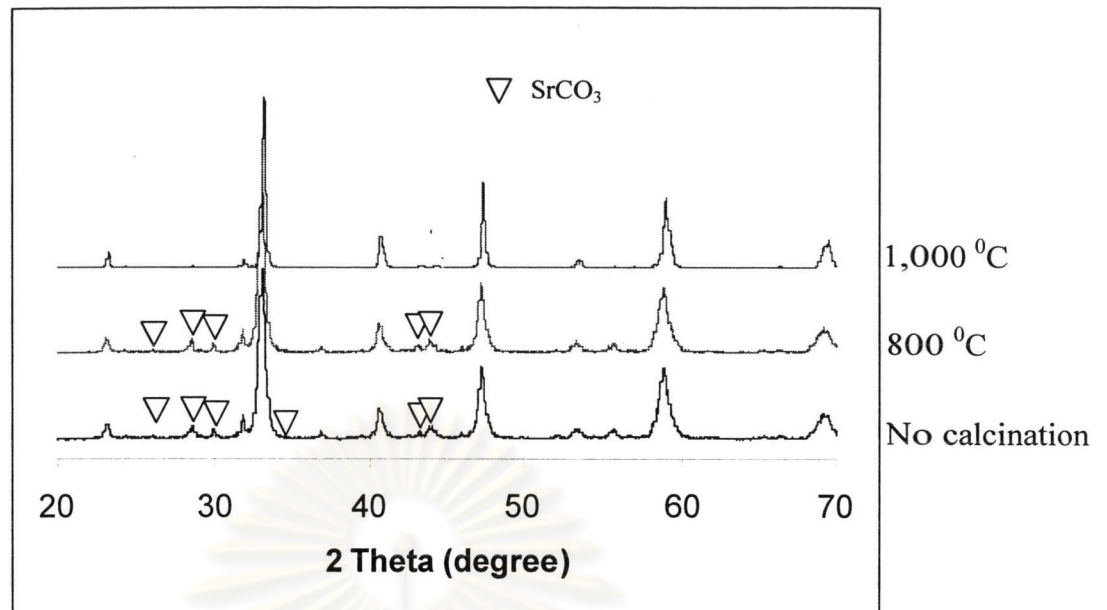
Figure 4.8 XRD patterns of LSC64 catalytic perovskite compound at various
calcination temperatures.

All calcined powders as well as uncalcined powder were examined by XRD in
order to investigate the phase development. From Figure 4.8, the XRD patterns of
uncalcined powder and powder calcined at 800 °C, showed the peaks of secondary
phase of $SrCO_3$ [JCPDS 05-0418] [60]. When the calcination temperature was
increase to 1,000 °C, the impurity disappeared. Therefore, it is to be noted that the
single phase of perovskite was successfully obtained in this work.

4.2.1.4 Crystal structure, unit cell data and crystalline phase analysis

A. **Crystalline phase analysis of $La_{1-x}Sr_xCoO_{3-\delta}$ (x = 0.2 - 0.6)**

From Figure 4.4, the XRD patterns show that when the Sr content in LSC was
higher than 0.4, the single phase perovskites with the cubic structure was obtained. To
indicate the formation of the perovskite-type phase with either a cubic or distorted
cubic structure, the diffraction peaks of LSC powders were observed within 2θ in the
range of $31°$ to $36°$ as shown in Figure 4.9. It can be noticed that the splitting peak of
orthorhombic between O (110) and O (104) reflections increase with the decrease of

strontium content while the composition with x ≤ 0.4 at the reflective plane 104 showed the orthorhombic phases.
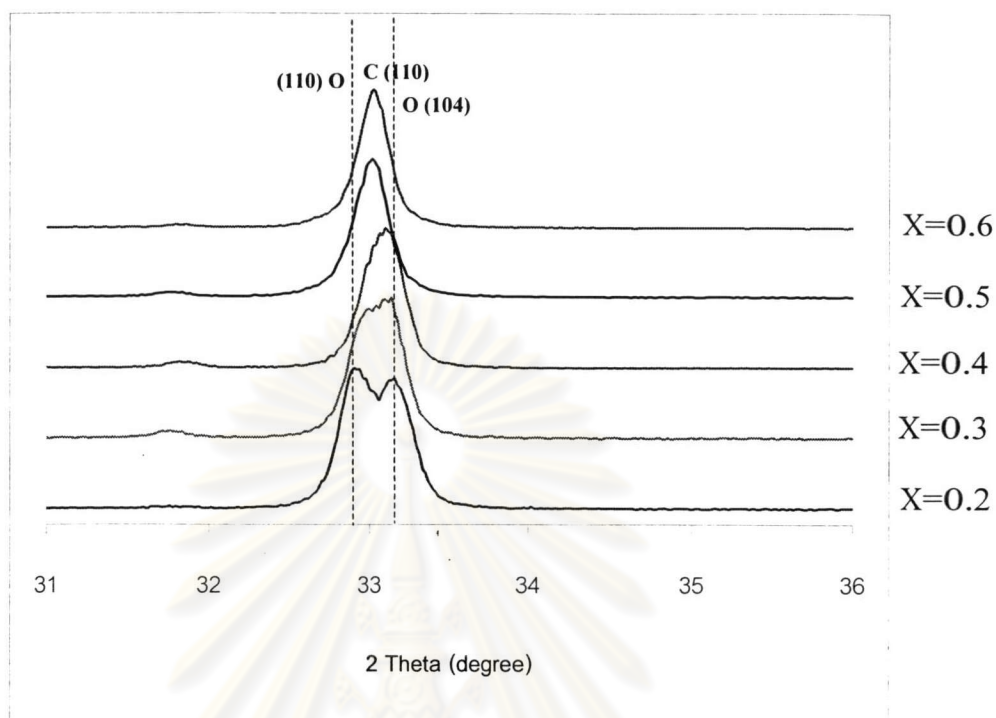
Figure 4.9 Characteristic splitting of the cubic c (110) into the o (110) and o (104) reflections of the orthorhombic cell during X-ray analysis of LSC.

This analysis shows that when the Sr content was higher than 0.5 (x = ≥ 0.5), the diffraction line at the reflective plane 110 of cubic structure was clearly presented.

The lattice parameters of $La_{1-x}Sr_xCoO_{3-\delta}$ (x = 0.2 - 0.6) catalytic perovskite compounds calculated from XRD data were listed in Table 4.7.

Table 4.7 Unit cell data from XRD patterns at room temperature for $La_{1-x}Sr_xCoO_{3-\delta}$ (x = 0.2 - 0.6)

x	Crystal system	a (Å)	b (Å)	c (Å)
0.2	Orthorhombic	3.8309	3.8689	3.8262
0.3	Orthorhombic	3.8260	3.8566	3.8384
0.4	Orthorhombic	3.8244	3.8382	3.8397
0.5	Cubic	3.8344	-	-
0.6	Cubic	3.8323	-	-

By comparing the unit cell volume values, it can be noticed that the unit cell volume is increased with an increasing of x due to the substitution of La^{3+} by Sr^{2+} (r_{La3+} = 1.36 Å, r_{Sr2+} = 1.44 Å in dodecahedral coordination) [61]. The substitution of La^{3+} ions with Sr^{2+} ions causes a significant increasing of c parameter and a small decreasing of a and b parameters. The decrease of a and b parameters could be explained by the presence of a part of cobalt ion in tetravalent state with smaller ionic radius, (r_{Co3+} = 0.75 Å, r_{Co4+} = 0.67 Å in octahedral coordination) as a result of electric charge compensation.

B. Crystalline phase analysis of $La_{1-x}Sr_xFeO_{3-\delta}$ (x = 0.2 - 0.6)

The phase analysis of $La_{1-x}Sr_xFeO_{3-\delta}$ (x = 0.2 - 0.6) observed by XRD within 2θ region 56°-60° was shown in Figure 4.10.
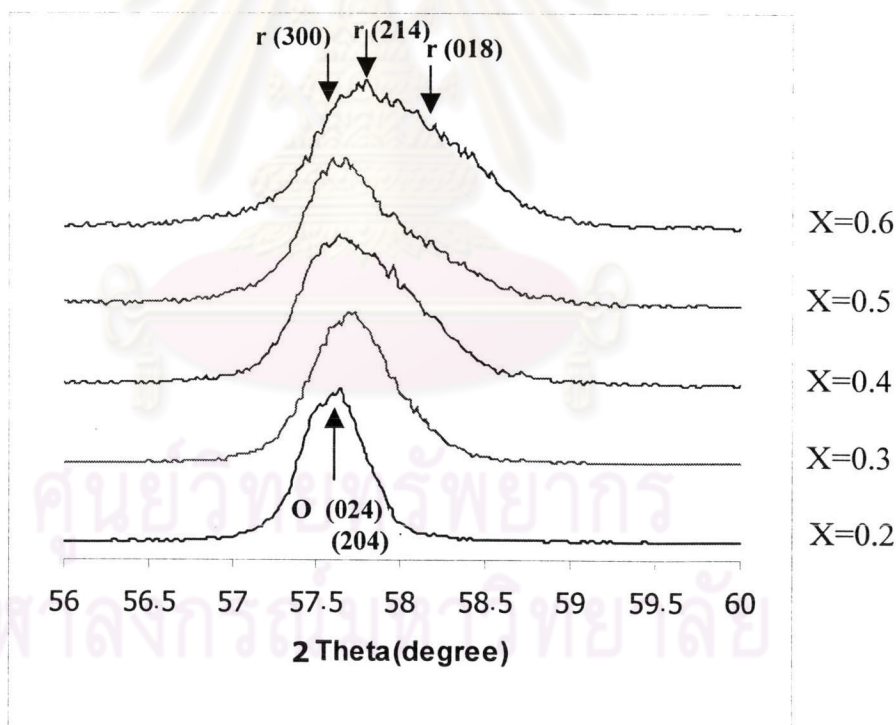
Figure 4.10 XRD patterns of $La_{1-x}Sr_xFeO_{3-\delta}$ showing the 2θ region in the range of 56°-60°.

It is clearly shown that the phase transformation from orthorhombic to rhombohedral has been observed with increasing of the Sr content. When the Sr

content in LSF was lower than 0.3 (X ≤ 0.3), the present of diffraction lines 024 and 204 was indicated that the powders had the orthorhombic structure. For $La_{1-x}Sr_xFeO_{3-\delta}$ with Sr content was higher than 0.4 (x ≥ 0.4), three reflection peaks (300, 214, and 018) of rhombohedral unit cell were exhibited.

The results of crystalline phase analysis of $La_{1-x}Sr_xFeO_{3-\delta}$ (x = 0.2 - 0.6) are summarized in Table 4.8.

Table 4.8 Unit cell data from XRD at room temperature for $La_{1-x}Sr_xFeO_{3-\delta}$ (x= 0.2 - 0.6)

x	Crystal system	a (Å)	b (Å)	c (Å)
0.2	orthorhombic	3.9175	3.9149	3.9232
0.3	orthorhombic	3.9126	3.8968	3.9244
0.4	rhombohedral	5.5278	-	13.4368
0.5	rhombohedral	5.5110	-	13.4157
0.6	rhombohedral	5.4762	-	13.4055

The phase transition from orthorhombic to rhombohedral structure has been observed with increasing Sr^{2+} substitution, for examples, both samples LSF82 and LSF73 have the orthorhombic structures. For x = 0.2 - 0.3, all peaks could be indexed on the basis of an orthorhombic unit cell, where x = 0.4 - 0.6 it showed a rhombohedral unit cell.

For x = 0.2 – 0.3, the substitution of La^{3+} ions (r_{La3+} = 1.36 Å) with higher Sr^{2+} ions (r_{Sr2+} = 1.44 Å) cause a significant a small increasing of c parameter and decreasing of a parameters.

From the lattice parameters (a and c) of $La_{1-x}Sr_xFeO_{3-\delta}$ (x = 0.4 - 0.6), they were decreased with increasing the substitution of Sr for La at A-site. It might be concluded that the balance charge of Fe^{3+} in structure had the smaller ionic radius than Fe^{4+} (r_{Fe3+} = 0.55 Å, r_{Fe4+} = 0.58 Å).

C. Crystalline phase analysis of $Ba_{1-x}Sr_xCoO_{3-\delta}$ (x = 0.2 - 0.6)

Figure 4.11 shows the phase analysis of $Ba_{1-x}Sr_xCoO_{3-\delta}$ (x = 0.2 - 0.6) observed by XRD.
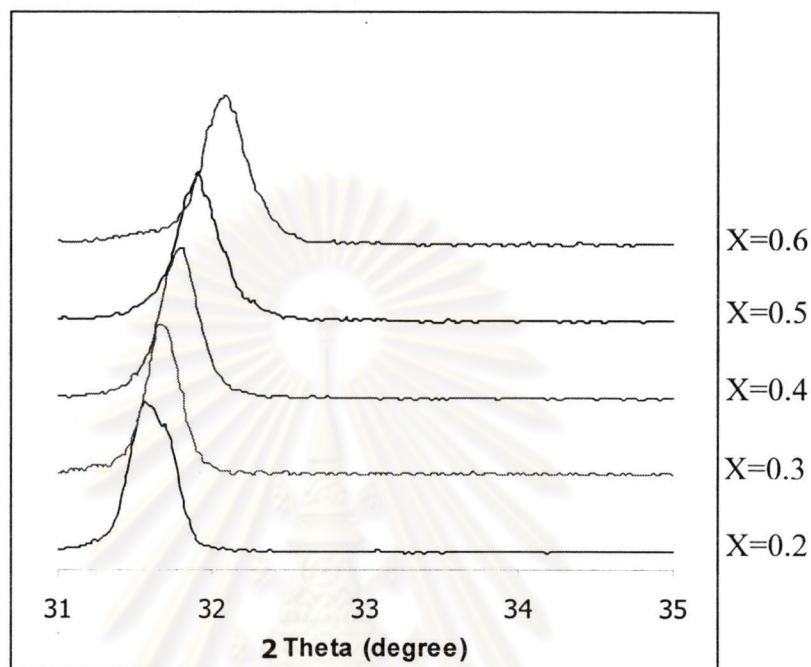
Figure 4.11 XRD patterns for hexagonal unit cell of $Ba_{1-x}Sr_xCoO_{3-\delta}$ (x = 0.2 - 0.6).

All the observed XRD peaks at x = 0.2 - 0.6 were indexed on the basis of the hexagonal unit cell as compared to $BaCoO_3$ (x = 0) reported previously [62]. The peak width was shown to enlarge with increasing Sr content in the hexagonal phase.

From the XRD, the refined unit cell parameters are calculated.

Table 4.9 Unit cell data from XRD at room temperature for $Ba_{1-x}Sr_xCoO_{3-\delta}$ (x = 0.2 - 0.6)

x	Crystal system	a (Å)	b (Å)	c (Å)
0.2	Hexagonal	5.4260	-	29.3545
0.3	Hexagonal	5.6850	-	31.7671
0.4	Hexagonal	5.8595	-	30.3358
0.5	Hexagonal	5.8368	-	30.2666
0.6	Hexagonal	5.8214	-	30.1217

These results showed that all the synthesized BSC compounds have hexagonal unit cell. For the $Ba_{1-x}Sr_xCoO_{3-\delta}$ (x = 0.2 - 0.3), the substitution of Ba^{3+} ions with Sr^{2+} ions were caused a significant increasing of a and c parameters. The increasing of a and c parameters could be explained by the presence of a secondary phase in structure. Unexpected results were found in x = 0.2 – 0.3, they would not considered in the further research. For the x = 0.4 – 0.6, the results showed that single phase perovakite, which indicated that the a and c lattice parameter decreased with increasing Sr content. Because radius of Sr^{3+} ion less than Ba^{2+} ion (r_{Sr2+} = 1.44 Å and r_{Ba2+} = 1.61 Å).

D. Crystalline phase analysis of $Ba_{1-x}Sr_xFeO_{3-\delta}$ (x = 0.2 - 0.6)

Figure 4.12 shows the variation of X-ray diffraction data of the orthorhombic (o) phase with in 2θ region 31°-36°.
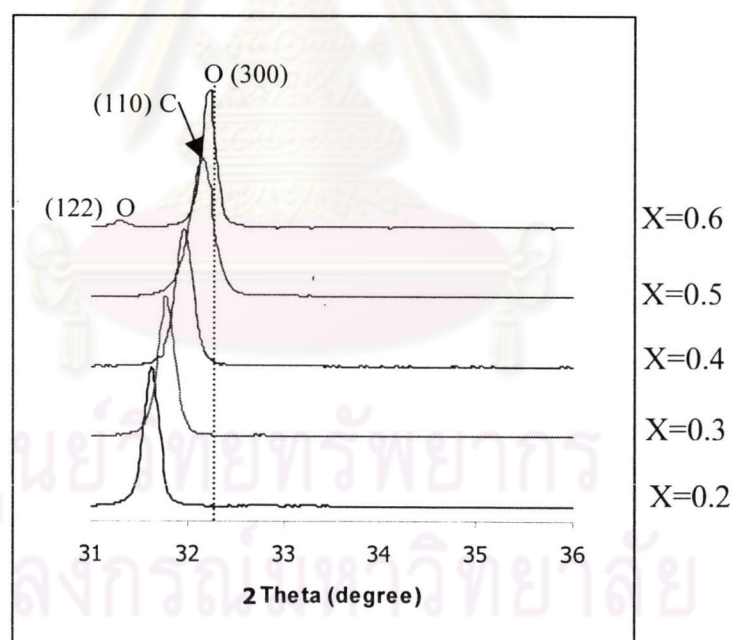
Figure 4.12 X-ray diffraction data of BSF showing the 2θ region 31°-36°.

The XRD patterns of $Ba_{1-x}Sr_xFeO_{3-\delta}$ with x ≤ 0.5 showed the cubic perovskite structure. The cubic unit cell due to c (110) reflection of BSF was observed within 2θ region the range of 31° - 36°. For the BSF46 which has unknown phases, showed

orthorhombic (o) phase which was confirmed by X-ray diffraction angles of (300) characteristic peak.

Table 4.10 lists both crystal structures and unit cell data of the $Ba_{1-x}Sr_xFeO_{3-\delta}$ (x = 0.2 - 0.6) perovskites.

Table 4.10 Unit cell data from XRD patterns at room temperature for $Ba_{1-x}Sr_xFeO_{3-\delta}$ (x = 0.2 - 0.6)

x	Crystal system	a (Å)	b (Å)	c (Å)
0.2	Cubic	3.9979	-	-
0.3	Cubic	3.9778	-	-
0.4	Cubic	3.9567	-	-
0.5	Cubic	3.9331	-	-
0.6	Orthorhombic	3.9296	3.9279	3.9198

It was found that all powders had the cubic unit cell, except BSF 46 had an orthorhombic unit cell. The values of the lattice parameter (a) tended to decrease in the presence of Sr in the $BaFeO_3$ lattice. This decrease in the a-value may be ascribed to the replacement of the Ba^{2+} ion (r_{Ba2+} = 1.61 Å) by a relatively smaller Sr^{2+} ion (r_{Sr2+} = 1.44 Å) in the oxide matrix.

4.2.1.5 Characterization of coated membranes

XRD patterns of the LSC64 layer coated on BSCF5582 membrane are compared with those of pure LSC64 and BSCF5582 powders, as shown in Figure 4.13.
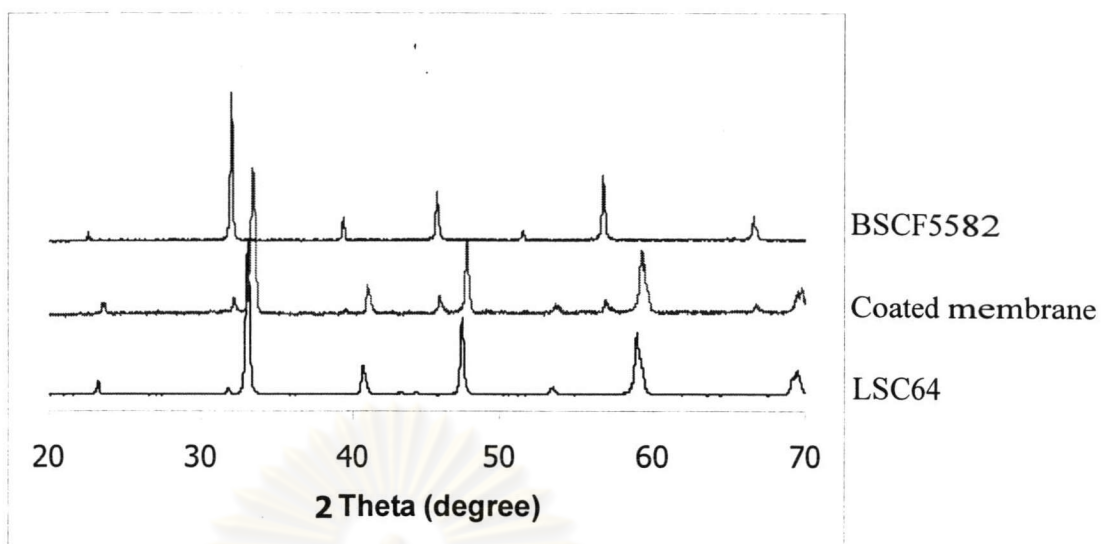
Figure 4.13 XRD patterns of pure and coated membrane. (a) Pure LSC64 powder;
(b) Coated membrane; (c) Pure BSCF5582 powder.

The pure LSC64 and BSCF5582 phases exhibit the different perovskite structure, orthorhombic and cubic structure, respectively with XRD peaks in different 2θ values.

The LSC64-BSCF5582 coated membrane, however, does exhibit the XRD patterns containing those of the two pure LSC64 and BSCF5582 phases.

From XRD analyses, the catalytic perovskite compounds with only single-phase structure were selected for coating. Therefore, LSC64, LSC55, LSC46; LSF82, LSF73; BSC64, BSC55, BSC46; and BSF82, BSF73, BSF64, BSF55 were coated onto LSCF8264 and BSCF5582 membranes. LSGF6437 membrane was coated with LSC64, LSC55, LSC46; and LSF82, LSF73, respectively.

4.2.2 Scanning electron microscope (SEM)

The morphologies of all the coated membranes sintered at different temperatures, were examined by SEM.

4.2.2.1 The effect of sintering temperature on coated membrane

The SEM pictures of LSC64 coated on LSCF8264, BSCF5582, and LSGF6437 membranes after sintering at 800 $^{\circ}$C, 1,000 $^{\circ}$C, and 1,100 $^{\circ}$C, respectively are shown in Figures 4.14, 4.15, and 4.16.
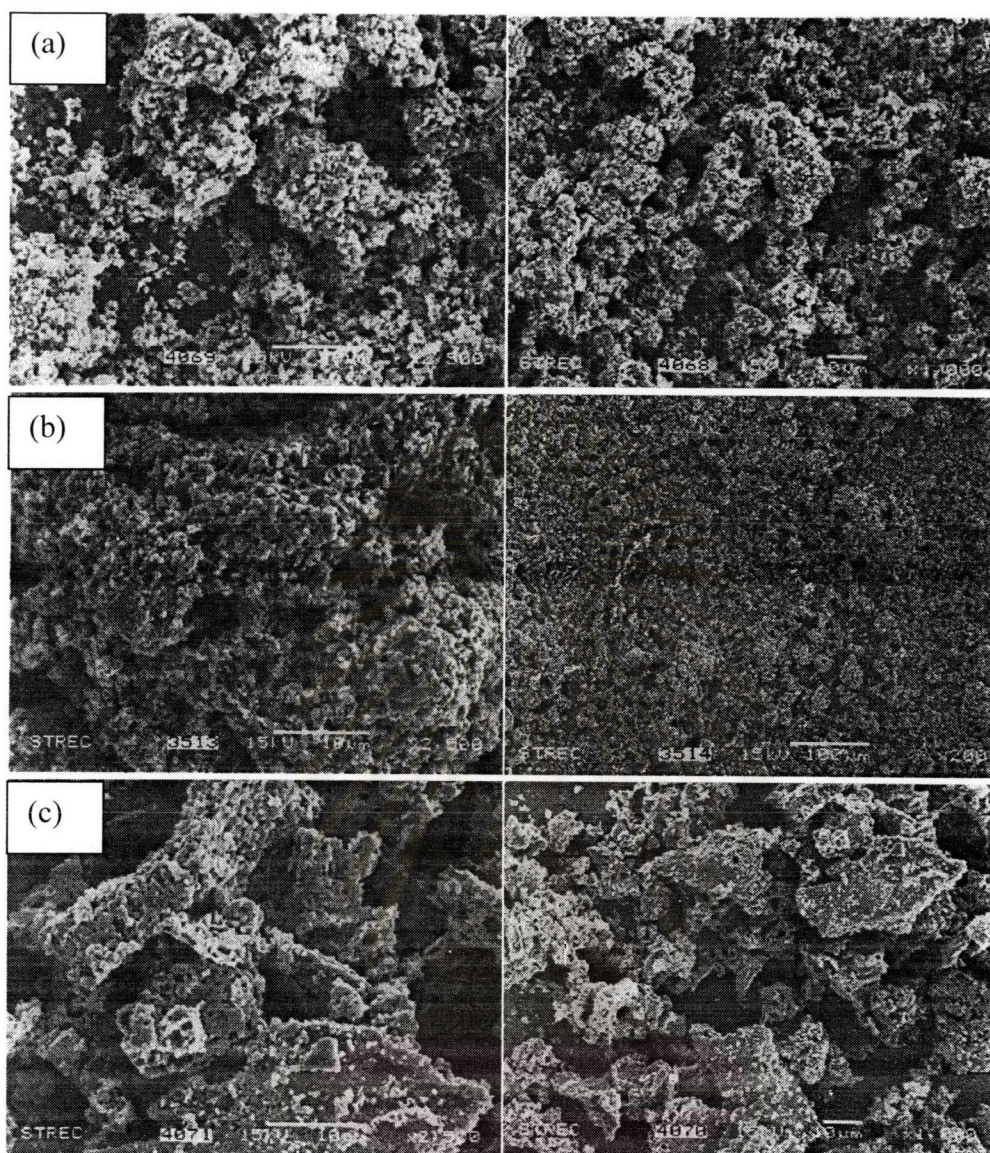
Figure 4.14 SEM pictures of top view of LSC 64 layer coat on LSCF 8264 membrane sintered at (a) 800 $^{\circ}$C, 5h. (b) 1,000 $^{\circ}$C, 5h. (c) 1,100 $^{\circ}$C, 5h.

In Figure 4.14, the left-hand picture shows the morphology of LSC64 coated on LSCF8264 membrane at high resolution (x2500), while the right-hand one shows morphology at low resolution (x1000). SEM pictures of LSC64-layer coated on membrane sintered at 800 $^{\circ}$C (Figure 4.14a), showed that the microstructure is ununiform and not agglomerate. The specimen treated at 1,000 $^{\circ}$C showed porous, particulate-composed LSC64 microstructure deposited on surface of membrane as shown in Figure 4.14b. The microstructure is uniform, there are noticeable gaps between particles and overall particle boundaries are distinct. This sample reveals

only initial stages of neck formation between the grains. Figure 4.14c displayed the morphology of coated membrane sintered at 1,100 °C. The irregular-shaped pores were observed which lead to increase in density more than the other coated membrane sintered at 800 °C and 1,000 °C.
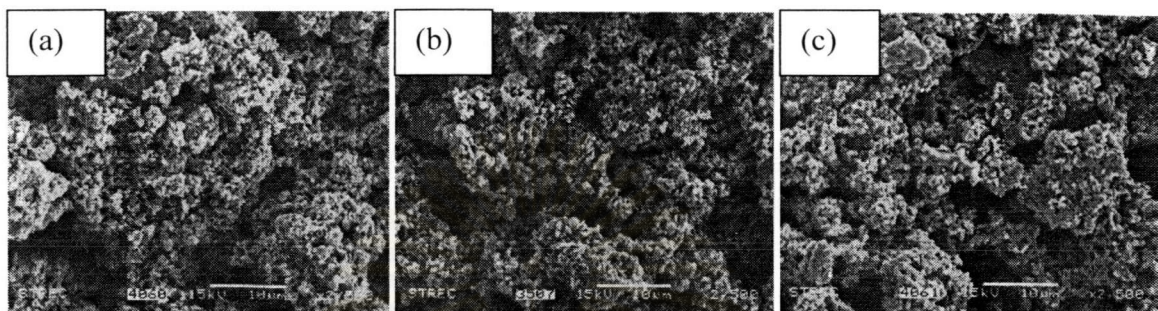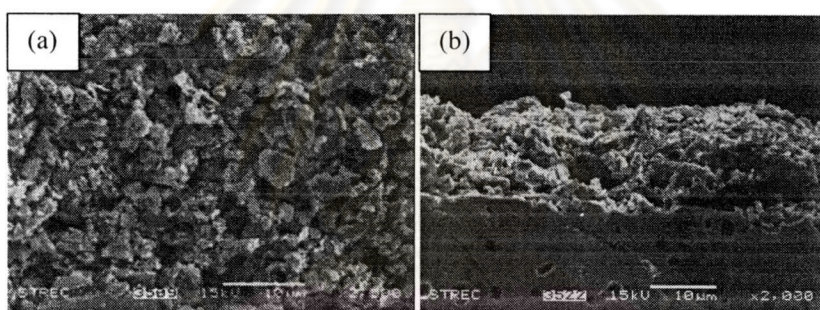

Figure 4.15 SEM pictures of top view of LSC 64 layer coat on BSCF 5582 membrane sintered at (a) 800 °C, 5h. (b) 1,000 °C, 5h. (c) 1,100 °C, 5h.

The LSC64-layer coated on BSCF5582 sintered at 1,000 °C is shown in Figure 4.15b, which exhibits similar morphology to that of coated LSCF8264 membrane.

Figure 4.16, shows porous layer of LSC64 coated on LSGF membrane at various sintering temperatures.
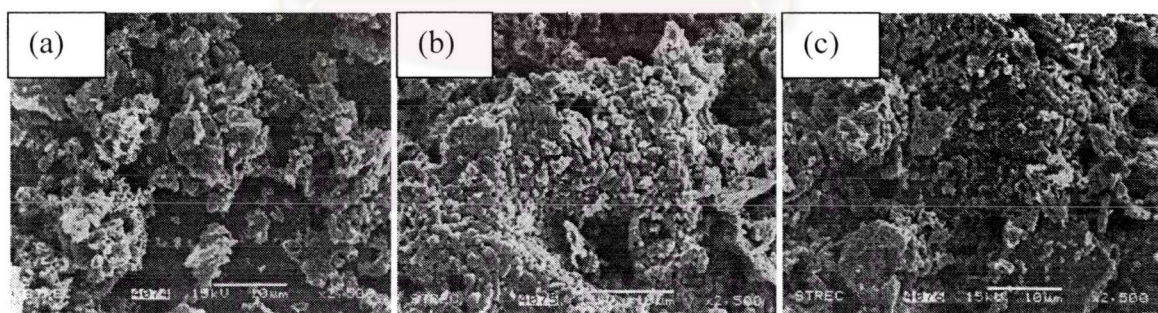
Figure 4.16 SEM pictures of top view of LSC 64 layer coat on LSGF 6437 membrane sintered at (a) 800 °C, 5h. (b) 1,000 °C, 5h. (c) 1,100 °C, 5 h.

The catalytic perovskite compounds LSC64 which coated on the three membranes exhibited porous microstructure at 1000 °C.

The top and cross view of the catalytic perovskite compounds were presented, including LSC64, LSF73, BSC55, and BSF55 layers were coated on BSCF5582 membrane were shown in Figures 4.17, 4.18, 4.19, and 4.20.
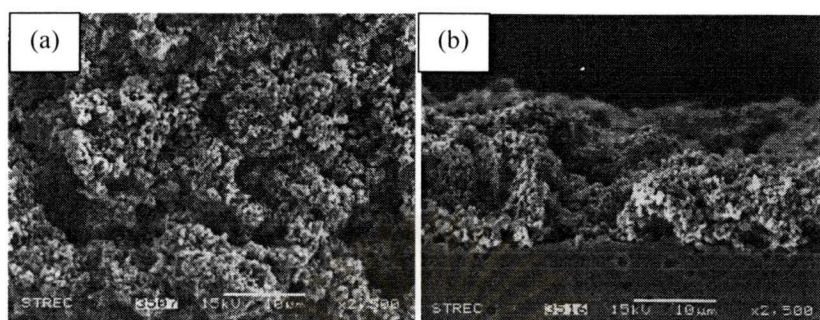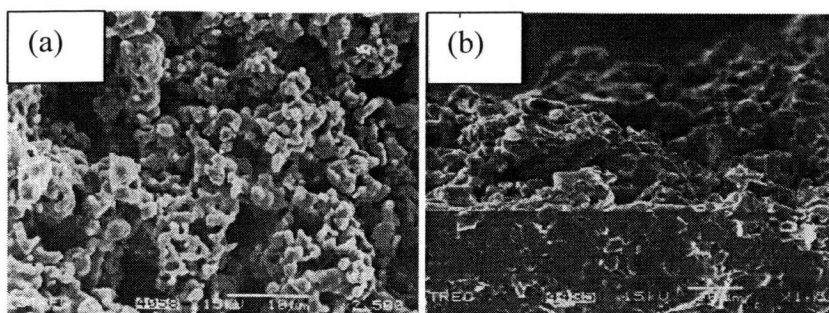

Figure 4.17 SEM pictures of top view of LSC 64 layer coat on BSCF 5582 membrane sintered 1,000 $^{\circ}$C, 5h. (a) top view (b) cross section

Figure 4.18 SEM picture of top view of LSF 73 layer coat on BSCF 5582 membrane sintered at 1000 $^{\circ}$C, 5 h. (a) and cross section (b).
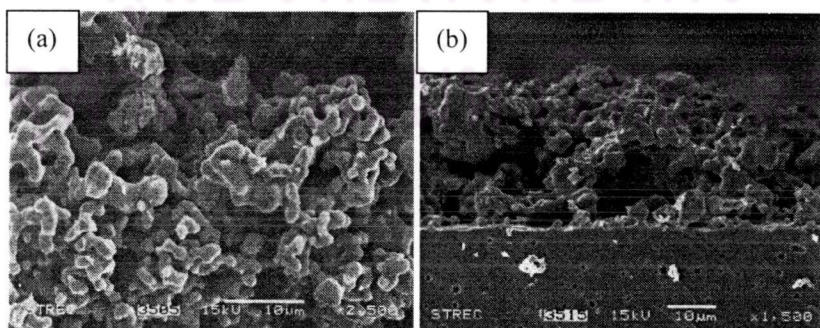
Figure 4.19 SEM picture of top view of BSC 55 layer coat on BSCF 5582 membrane sintered at 1000 $^{\circ}$C, 5h.(a) and (b) cross section.

Figure 4.20 SEM picture of top view of BSF 55 layer coat on BSCF 5582 membrane sintered at 1000 $^{\circ}$C, 5h. (a) and (b) cross section.

Figure 4.17b shows the cross section of LSC64-layer coated on BSCF 5582. It is exhibited that the grain neck formation of particles appears. It can be seen that the boundary exist between porous coating layer and dense membrane. SEM photoghaph, all pictures were indicated same results of the porous layer at sintered 1,000 $^{\circ}$C.

From the SEM results, it is concluded that the optimum sintering temperatures for all the LSCF8264, BSCF5582, and LSGF6437 coated membranes are 1,000 $^{\circ}$C.

4.2.2.2 The coated membranes (BSCF5582, LSCF8264, and LSGF6437) with various catalytic perovskite compounds

A. $Ba_{0.5}Sr_{0.5}Co_{0.8}Fe_{0.2}O_{3-\delta}$ (BSCF 5582) membrane

The catalytic perovskite compounds including LSC, LSF, BSC, and BSF perovskite oxides were coated on BSCF membrane. The results were presented in Figures 4.21, 4.22, 4.23 and 4.24.
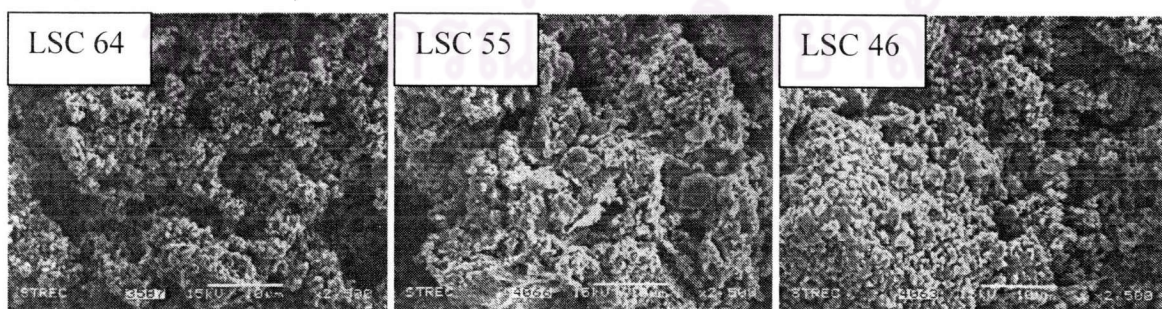
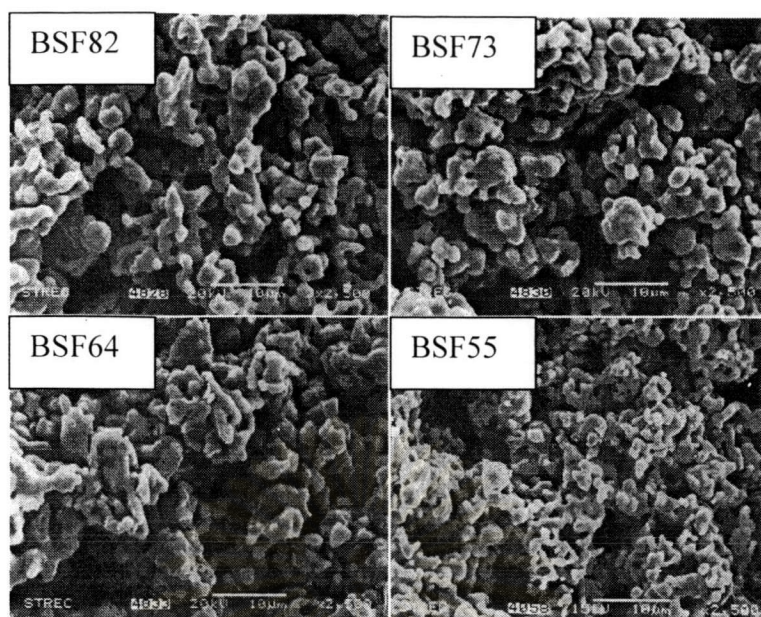**Figure 4.21** SEM pictures of top view of BSCF 5582 membrane coated by LSC 64, LSC 55, and LSC 46 sintered at 1,000 $^{\circ}$C, 5h.
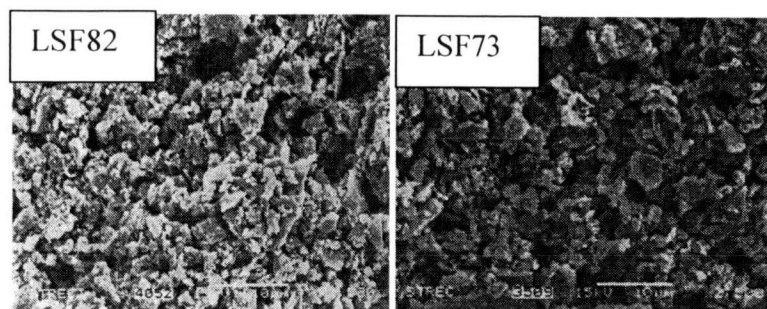
Figure 4.22 SEM pictures of top view of BSCF 5582 membrane coated by
LSF 82 and LSF 73 sintered at 1,000 ^{o}C, 5h.

Figure 4.23 SEM pictures of top view of BSCF 5582 membrane coated by
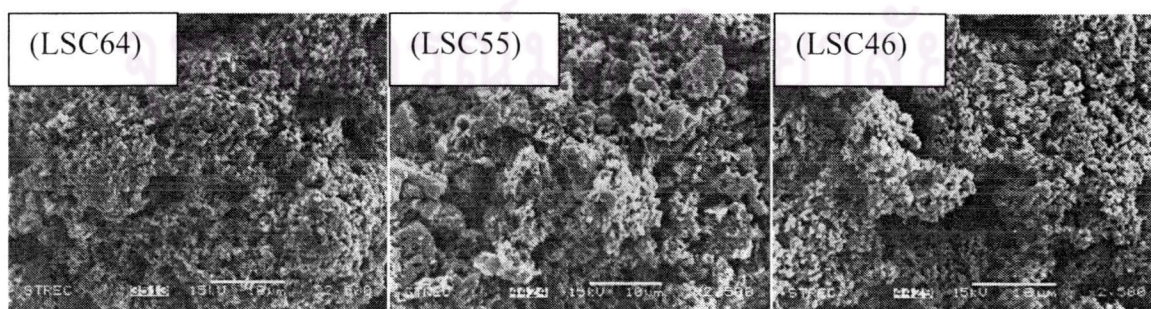BSC 64, BSC 55, and BSC 46 sintered at 1,000 ^{o}C, 5h.

Figure 4.24 SEM pictures of top view of BSCF 5582 membrane coated by
BSF 82, BSF 73, BSF 64, and BSF 55 layer sintered at 1,000 ^{o}C, 5h.

SEM photographs of the coated layer reveal porous structure which were obtained at sintering temperature 1,000 ^{o}C.

## B. $La_{0.8}Sr_{0.2}Co_{0.6}Fe_{0.4}O_{3-\delta}$ (LSCF 8264) membrane

The microstructures of catalytic perovskite compounds at different compositions of metals coated on LSCF membrane, were studied by SEM. SEM micrographs of all coating layers clearly showed the porous structure in Figures 4.25, 4.26, 4.27, and 4.28, respectively.
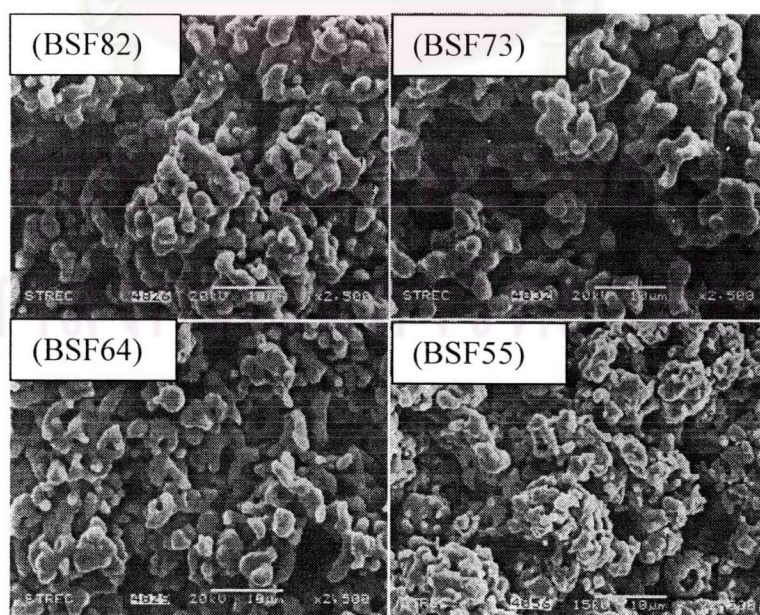

Figure 4.25 SEM pictures of top view of LSCF 8264 membrane coated by
LSC 64, LSC 55, and LSC 46 layer sintered at 1,000 ^{o}C, 5h.
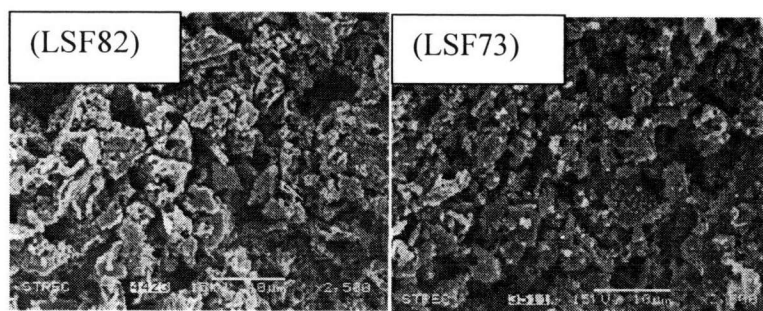
Figure 4.26 SEM pictures of top view of LSCF 8264 membrane coated by LSF 82 and LSF 73 layer sintered at 1,000 °C, 5h.
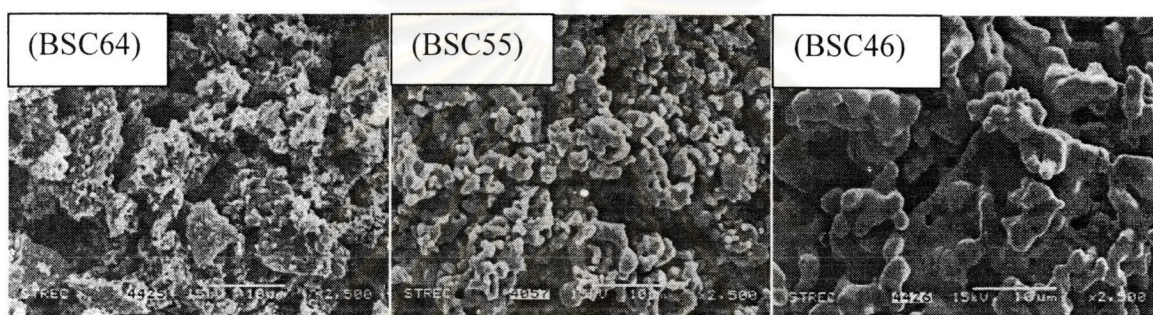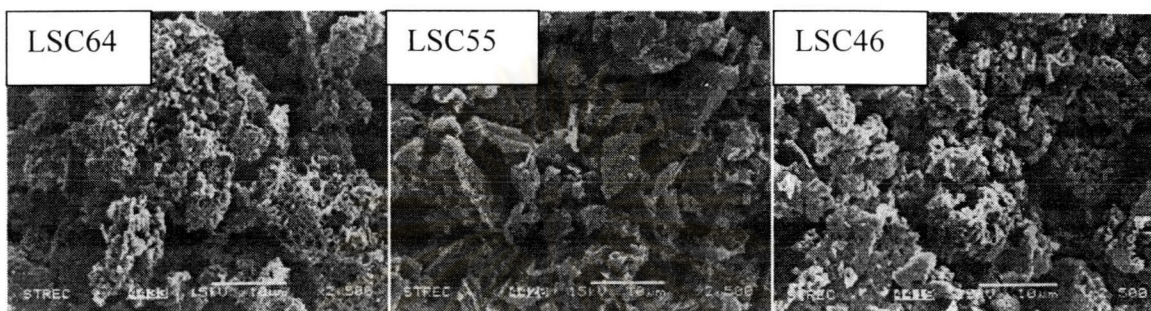

Figure 4.27 SEM pictures of top view of LSCF 8264 membrane coated by BSC 64, BSC 55, and BSC 46 layer sintered at 1,000 °C, 5h.
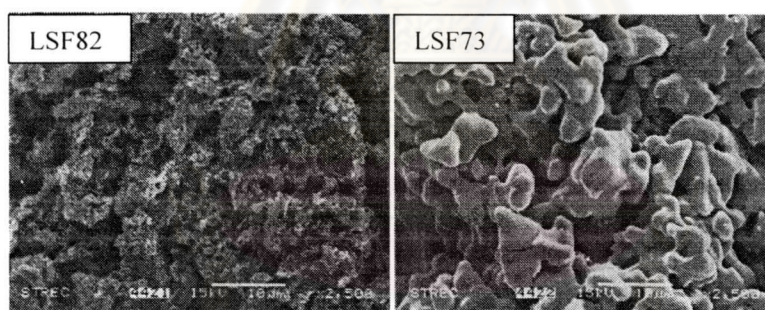

Figure 4.28 SEM pictures of top view of LSCF 8264 membrane coated by BSF 82, BSF 73, BSF 64, and BSF 55 layer sintered at 1,000 °C, 5h.

C. $La_{0.6}Sr_{0.4}Ga_{0.3}Fe_{0.7}O_{3-\delta}$ (LSGF 6437) membrane

Figure 4.29 and 4.30 shows the coating layer onto LSGF membrane. The SEM photographs of the series of LSC and LSF compounds were shows the coating on the LSGF membrane.

Figure 4.29 SEM pictures of top view of LSGF 6437 membrane coated by LSC 64, LSC 55, and LSC 46 layer sintered at 1,000 ^{o}C, 5h.

Figure 4.30 SEM pictures of top view of LSGF 6437 membrane coated by LSF 82 and LSF 73 layer sintered at 1,000 ^{o}C, 5h.

The results showed the porous structure of catalytic perovskite oxide coated onto the LSGF6437 membrane.

4.3 Oxygen desorption of perovskite compounds

4.3.1 Thermogravimetric analysis (TGA) method

Thermogravimetric temperature experiments were conducted to measure the oxygen desorption and adsorption of the coated membrane. Based on thermal analysis, about 20 mg of such calcined powders (substrate and catalytic perovskite compounds) was used for this analysis.

Figure 4.31 shows the TGA curve of the BSF55 powder after calcined.
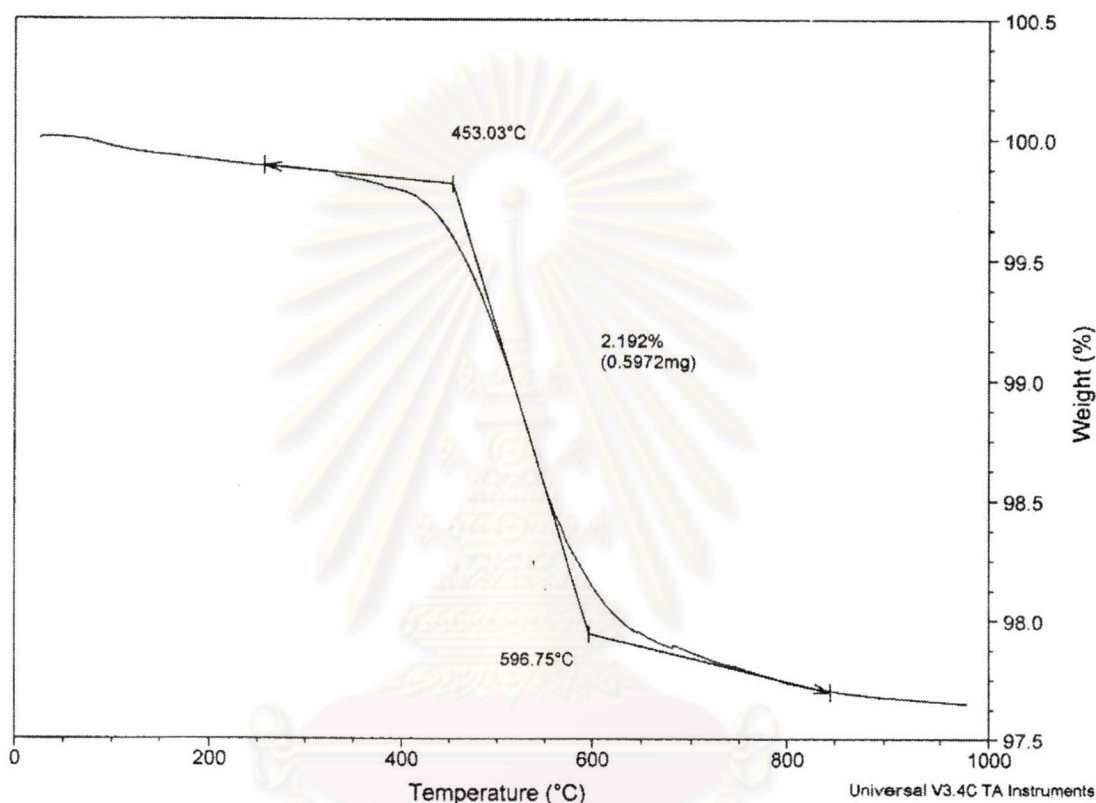
Figure 4.31 TGA thermogram of $Ba_{0.5}Sr_{0.5}FeO_{3-\delta}$ (BSF55) powder

The oxygen desorption of BSF55 was presented in Figure 4.31. It can be seen that, the amount of oxygen was desorbed during the thermogravimetric analysis. A remarkable weight loss is observed which corresponds to oxygen desorption relating to oxygen vacancy concentration in the perovskite material [53]. It is found that the oxygen desorption beginning at about 453 °C and the weights of sample changed rapidly when the temperature increases.

TGA data of the uncoated and coating perovskites are listed in Table 4.11.

Table 4.11 TGA data of the perovskite compounds

Sample	Onset Temperature (^{o}C)	1st Weight loss %
LSCF8264	330	0.0254
LSGF6437	349	0.0764
BSCF5582	379	1.2360
LSC 64	330	0.2602
LSC 55	269	0.5760
LSC 46	291	0.6746
LSF 82	330	0.1243
LSF 73	344	0.1320
BSC 64	320	1.0980
BSC 55	360	0.8386
BSC 46	350	1.1450
BSF 82	494	1.4600
BSF 73	507	1.5280
BSF 64	483	1.8530
BSF55	453	2.1920

Condition; Room temperature to 1,000 ^{o}C rate 20 ^{o}C/min

From TGA result the first onset of loss of O_2 was about 300-400 ^{o}C for all composition. No further weight loss appears thereafter, whereas a thermal decomposition of residual water and organic component after calcination of the perovskite powder can be seen in the TGA curve. It is concluded that the highly Sr-doped Ba- and La-based perovskite compounds with highest oxygen desorption owing to its high oxygen vacancy.

The BSCF5582 substrate perovskite compounds had excellence of oxygen desorption properties (1.236 %) as compared to LSCF8264 and LSGF6437, (0.0764 % and 0.0254 %).

As listed in Table 4.11 the measured oxygen desorption of the catalytic perovskite compounds BSF55 is higher than those of the other oxides. It is reported

elsewhere [54] that the oxygen permeation flux is correlated to the data measured by TGA. It is concluded that BSF55 has highest oxygen permeation flux.

4.3.2 Temperature-program desorption of oxygen (O$_2$-TPD)

The adsorption-desorption property of the catalytic perovskite plays an important role in the reaction on surface. Note that there are two kinds of oxygen, the so-called α and β-oxygen, these desorbed at low temperature and high temperature, respectively.

In the theory [57], the change in valence state of the metal ions in perovskite is usually accompanied with the oxygen desorption, which can be detected by thermal conductivity detector (TCD, from O$_2$–TPD technique). At moderate temperature range (usually ~200 - 600 ^{o}C), the oxygen desorption peak usually associates with the reduction of high valene state Co^{4+} to Co^{3+}.

Usually, at a temperature higher than 800 ^{o}C, the tri-valence state Co^{3+} can be reduced to a lower Co^{2+}, accompanied by the desorption of oxygen.
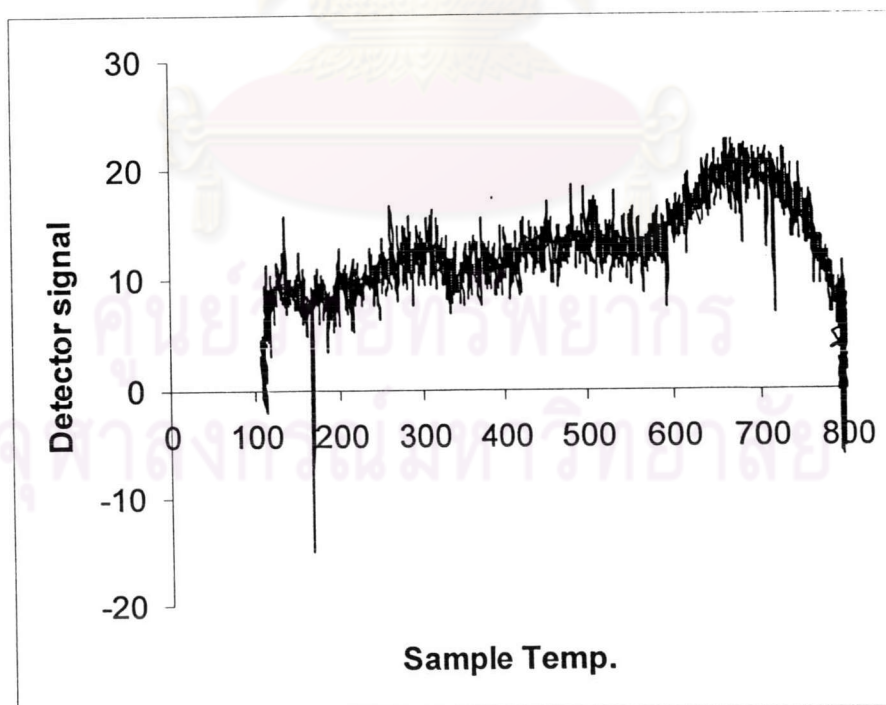
4.3.2.1 The O$_2$–TPD of the substrate perovskite compounds

The O$_2$–TPD profiles of LSCF8264, LSGF6437, and BSCF5582 substrate perovskite compounds are shown in Figure 4.32 (a), (b), and (c), respectively.
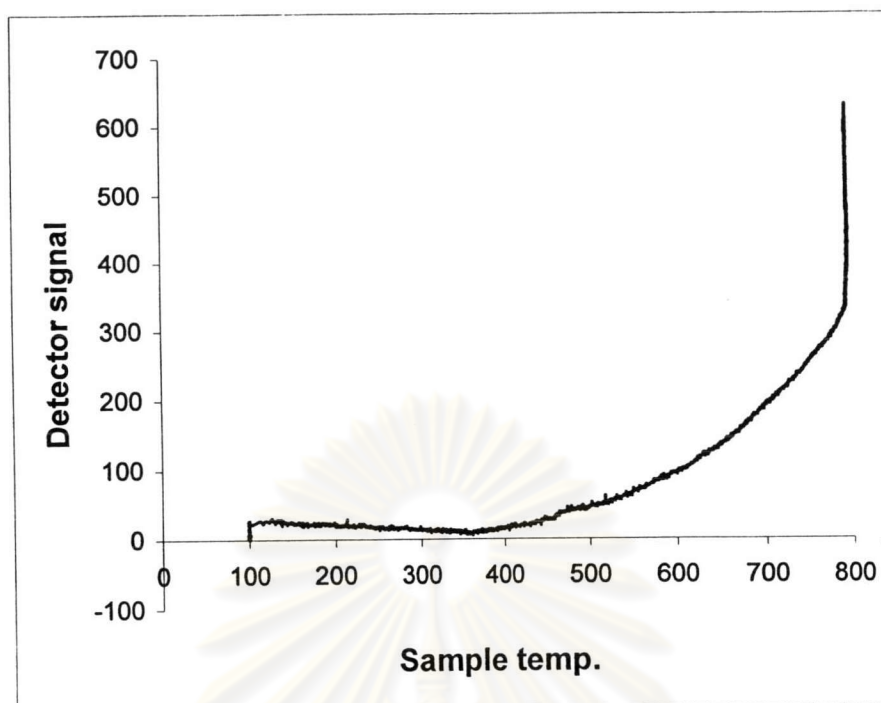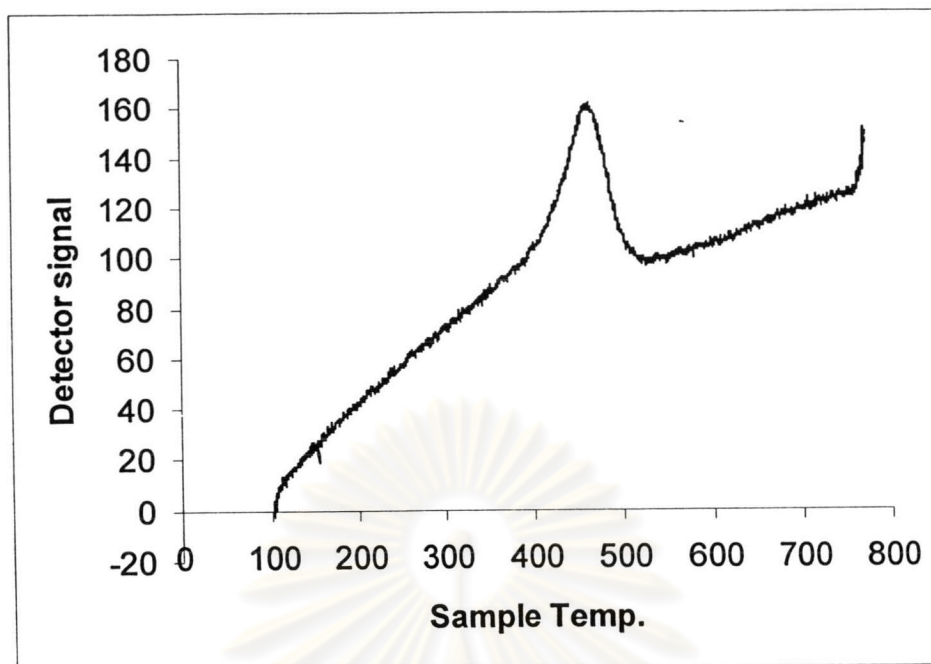
(a) $La_{0.8}Sr_{0.2}Co_{0.6}Fe_{0.4}O_{3-\delta}$ (LSCF8264)

(b) $La_{0.6}Sr_{0.4}Ga_{0.3}Fe_{0.7}O_{3-\delta}$ (LSGF6437)

(c) $Ba_{0.5}Sr_{0.5}Co_{0.8}Fe_{0.2}O_{3-\delta}$ (BSCF5582)

Figure 4.32 The O_2–TPD profiles of the substrate perovskite compounds:
(a) LSCF8264, (b) LSGF6437, and (c) BSCF5582, respectively.

O_2–TPD technique provides an effective way to investigate the oxygen properties of perovskite materials.

The peak area LSCF8264 in the low temperature zone was much smaller than those of LSGF6437 and BSCF5582. An addition, the TPD signal of BSCF5582 in Figure 4.32 (c) shows a sharp peak at the low temperature zone ~ 400 °C.

Eventually, the oxygen desorption of different substrate perovskite compounds decreased in the following order: BSCF5582 > LSGF6437 > LSCF8264.

4.3.2.2 The O_2–TPD of the catalytic perovskite compounds

The O_2-TPD profiles for $La_{1-x}Sr_xCoO_3$ (x = 0.4 - 0.6) catalytic perovskites are shown in Figure 4.33.
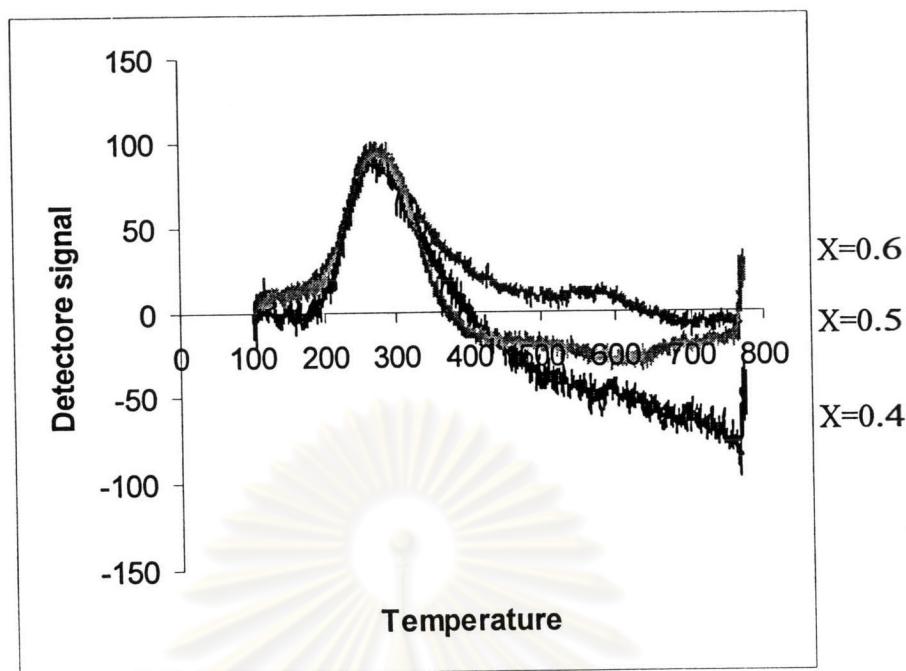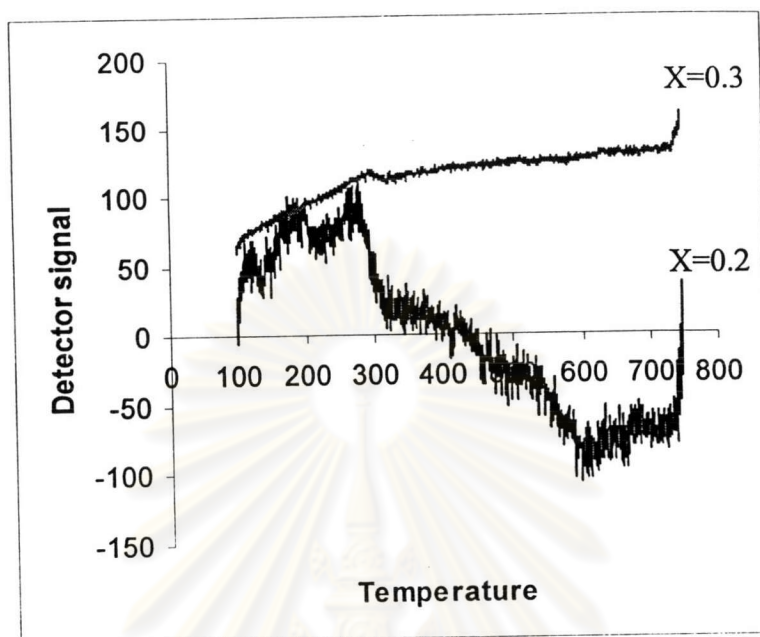
Figure 4.33 O_2-TPD profiles over $La_{1-x}Sr_xCoO_{3-\delta}$ (x = 0.4 - 0.6).

Figure 4.33 shows TPD chromatograms of oxygen of LSC64, LSC55, and LSC46. All the samples exhibited relatively sharp desorption peaks just above 200 °C, which has been collectively called as the α-desorption. The amount of the α-desorption increased with increasing the substitution level of Sr for La at A-site, LSC64 < LSC55 < LSC46.

From the O_2-TPD profiles, it could be concluded that the amount of α- oxygen desorbed at the low temperature zone (~300) increased with the increase of doping content of Sr in LSC. The largest amount of α-oxygen desorbed at the high temperature zone (~800) changed only a little when x ≥ 0.5. In the series of LSC mixed oxides, when the tri-valence ion La^{3+} at A site is substituted by a lower valence ion Sr^{2+}, according to the electroneutrality, the positive charge reduction could be balanced either by the formation of higher oxidation state ion at B site, i.e. $Co^{2+} \rightarrow Co^{3+}$ or by the formation of oxygen vacancy (Vo) [63]. So the contents of Co^{3+} and oxygen vacancy (V_o) increase with the increase of x, and the charge of the mixed oxides is mainly balanced by the increasing of oxygen vacancy. Actually, well correlation between the TGA data and the relatively oxygen desorption was observed.

The O_2-TPD curves were obtained over $La_{1-x}Sr_xFeO_{3-\delta}$ (x = 0.2 - 0.3) as shown in Figure 4.34.
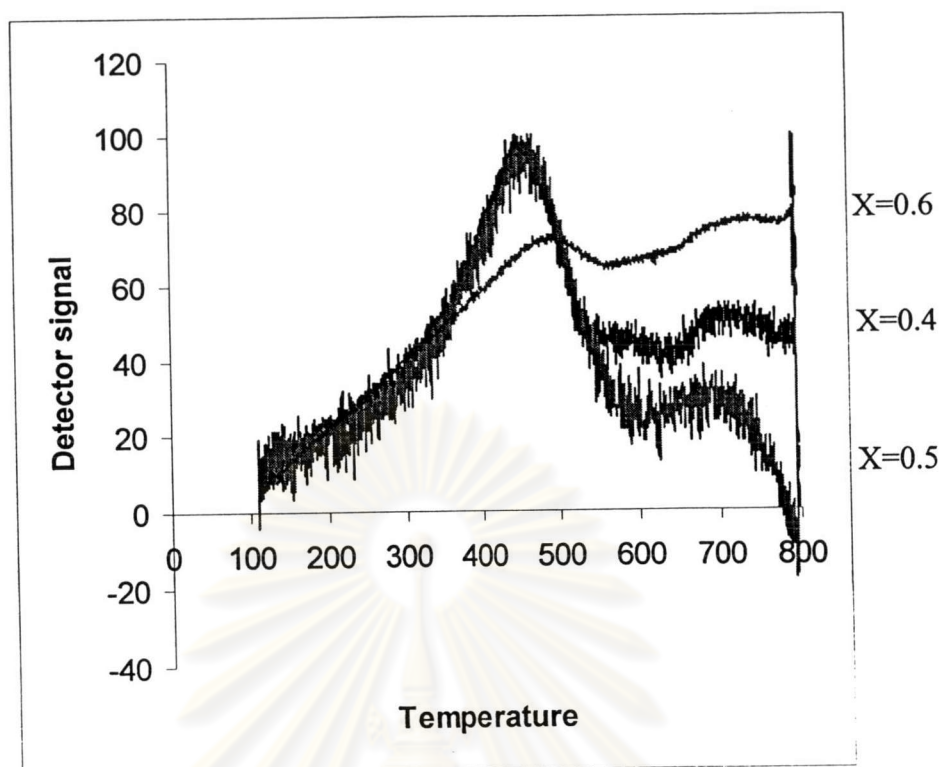

Figure 4.34 O_2-TPD profiles over $La_{1-x}Sr_xFeO_{3-\delta}$ (x = 0.2 - 0.3).

In this study, the peak area was clearly observed that the LSF73 is much higher than LSF82. It is indicated the relatively oxygen desorption increased in order: LSF82 < LSF73, as a function of Sr content.

The O_2–TPD profiles of $Ba_{1-x}Sr_xCoO_{3-\delta}$ with varying Sr content are shown in Figure 4.35.

Figure 4.35 O_2-TPD profiles over $Ba_{1-x}Sr_xCoO_{3-\delta}$ (x = 0.4 - 0.6).

The O_2-TPD curves were obtained over $Ba_{1-x}Sr_xCoO_{3-\delta}$ (x = 0.4 - 0.6). There are two O_2–desorption peaks (α and β). α-peak (at ~300 ^{o}C) corresponds to desorption of the oxygen chemically adsorbed on oxygen vacancies [64], namely, the oxygen is released by reduction of B ion [65]. Therefore, β peak (at ~800 ^{o}C) might be attributed to the lattice oxygen associated with the reduction of B ions. Figure 4.35 shows that BSC46 have high oxygen desorption property. It could be suggested that BSC46 have an excellent oxygen permeability.

Conclusion can be made from the O_2–TPD results that the introduction of Sr in BSC can suppress the oxidation of Co^{3+} to Co^{4+} and make the reduction of Co^{4+} to Co^{3+} easier. The introduction of Ba^{2+} had little influence on the reduction of Co^{3+} to Co^{2+}.

The amounts of oxygen desorbed from $Ba_{1-x}Sr_xFeO_{3-\delta}$ with varying Sr contents were shown in Figure 4.36.
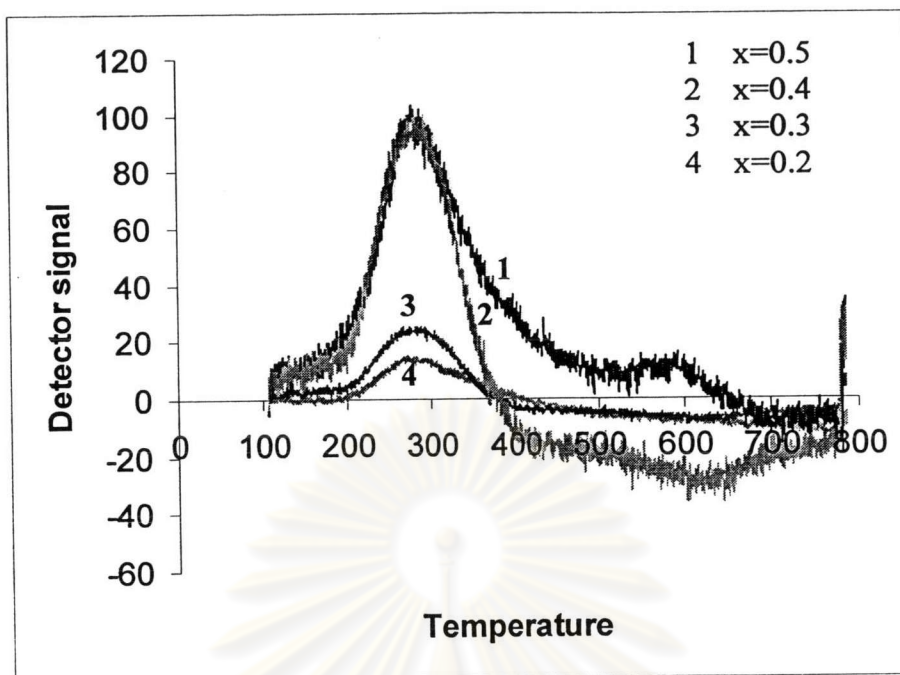
Figure 4.36 O_2-TPD profiles over $Ba_{1-x}Sr_xFeO_{3-\delta}$ (x=0.2-0.5).

The oxygen desorption peaks were observed for most of the reduced oxides for x = 0.5, which demonstated the first sharp desorption peak at temperature zone at ~200 °C. It was found that the amount of oxygen desorbed at this zone increased with increasing doping content of Sr (x), implying that the increase of oxygen vacancies, were obtained. The amount of the relatively sharp desorption peaks increased in order: BSF82 < BSF73 < BSF64 < BSF55.

In order to increase the oxygen permeation flux of the perovskite membrane. One way is to modify the surface of dense membrane by coating with the porous layer. From the oxygen desorption result, it was found that the BSF catalytic perovskite compounds is the best catalytic compound for coating on substrate membranes. Because its cubic structure is stable at high condition.

It is seen that the oxygen desorption capability of perovskite compounds obtained from TGA is consistent with that the O_2-TPD method.

It is suggested that BSF55 with the high oxygen desorption is the best choice to be coated on the BCSF5582, LSGF6437, and LSCF8264 membranes, respectively.